HHS Public Access

Author manuscript

Nat Nanotechnol. Author manuscript; available in PMC 2022 November 10.

Published in final edited form as:

Nat Nanotechnol. 2022 September ; 17(9): 1015–1022. doi:10.1038/s41565-022-01189-y.

Remotely controlled near-infrared triggered photothermal treatment of brain tumors in freely-behaving mice using gold nanostars

Hamed Arami[1,*,#], **Siavash Kananian**[2,#], **Layla Khalifehzadeh**[3,#], **Chirag B. Patel**[1,4,5], **Edwin Chang**[1], **Yuji Tanabe**[2,6,7], **Yitian Zeng**[8], **Steven J. Madsen**[8], **Michael J. Mandella**[1], **Arutselvan Natarajan**[1], **Eric E. Peterson**[9], **Robert Sinclair**[8], **Ada S. Y. Poon**[2,10,*], **Sanjiv Sam Gambhir**[1,11,$]

[1]Department of Radiology, Molecular Imaging Program at Stanford, Stanford School of Medicine, Stanford, CA.

[2]Department of Electrical Engineering, Stanford University, Stanford, CA.

[3]Department of Chemical Engineering, Stanford University, Stanford, CA.

[4]Department of Neuro-Oncology, The University of Texas MD Anderson Cancer Center, Houston, TX.

[5]Neuroscience Graduate Program, The University of Texas MD Anderson Cancer Center UT Health Graduate School of Biomedical Sciences (GSBS), Houston, TX.

[6]Aeterlink, Corp., Japan.

[7]AET, Inc., Japan.

[8]Department of Materials Science and Engineering, Stanford University, Stanford, CA.

[9]Department of Comparative Medicine, Stanford School of Medicine, Stanford, CA.

[10]Chan Zuckerberg Biohub, San Francisco, CA.

[11]Department of Bioengineering, Stanford University, Stanford, CA.

Abstract

[*]Corresponding Author: Hamed Arami, PhD. hamed.arami@asu.edu; Ada S. Y. Poon, PhD. adapoon@stanford.edu.
[$]Prof. Sanjiv Sam Gambhir passed away on July 18 2020.
[#]These authors contributed equally.

Author contributions: H.A. developed the idea, carried out or supervised all experiments, analyzed the data, and wrote the manuscript. H.A., S.K., and L.K. designed the project and experiments and contributed in data analysis and manuscript revision. C.B.P, E.C., and A.N. contributed to the animal experiments, imaging and histological data analysis and E.E.P. helped for tissue processing and histological experiments. Y.T. and A.S.Y.P discussed and supervised designing the wireless systems. Y.Z., S.J.M., and R.S. performed SEM. M.J.M. contributed in designing the optical devices. All authors reviewed and commented on the manuscript. S.S.G. and A.S.Y.P discussed and supervised experiments and manuscript preparations.

Competing interests: The authors declare the following competing interests: A.S.Y.P. and Y.T. cofound Aeterlink Corp. and Vivonda Medical Inc. commercializing wireless powering technology. H.A., S.K., L.K., M.J.M., A.S.Y.P., and S.S.G are the co-inventors of a patent covering this study filed by Stanford University. All the other authors have no competing interests.

Reporting summary. Further information on research design is available in the Nature Research Reporting Summary linked to this article.

Current clinical brain tumor therapy practices are based on tumor resection and post-operative chemotherapy or X-ray radiation. Resection requires technically challenging open skull surgeries that can lead to major neurological deficits and, in some cases, death. Treatments with X-ray and chemotherapy, on the other hand, cause major side-effects, such as damage to surrounding normal brain tissues and other organs. Here, we report development of an integrated nanomedicine-bioelectronics brain-machine interface that enables continuous and on-demand treatment of brain tumors, without open skull surgery and toxicological side-effects on other organs. Near-infrared surface plasmon characteristics of our gold nanostars enabled precise treatment of deep brain tumors in freely-behaving mice. Moreover, the nanostars' surface-coating enabled their selective diffusion in tumor tissues after intratumoral administration, leading to exclusive heating of the tumors for treatment. This versatile remotely controlled and wireless method allows for adjustment of nanoparticles photothermal strength, as well as power and wavelength of the therapeutic light to target tumors in different anatomical locations within the brain.

Introduction:

Conventional cancer therapy approaches such as chemo- and radiation-therapy combined with surgical resection, are inadequate for treating aggressive brain tumors (*e.g.*, glioblastoma multiforme, GBM). Despite standard-of-care surgery, radiation, and chemotherapy, the median overall survival for patients with glioblastoma is 16-21 months [1] with a 5-year survival rate of 5.6% [2]. This is mainly because of drug and radiation resistant nature of the GBM cells, which results in post-treatment tumor recurrence or metastasis. Controlled heating of the tumors has been used as an effective method for treatment of various tumors [3], and can potentially help to eradicate these treatment-resistant cells [4]. Therefore, developing less invasive and tumor targeted heating procedures such as nanoparticle-based photothermal therapy can offer opportunities for improved GBM treatment and prolonged survival.

Photothermal therapy with nanoparticles enables precise treatment of tumors, due to its capability for selective tumor irradiation and heating with minimal side-effects on surrounding tissues [5,6]. However, this technique is limited to single-session intraoperative treatment of tumors that are superficial to the affected organs, since their targeted tumors need to be exposed by an open surgery to activate light-triggered therapeutic reactions [6]. This is a major technical challenge for treatment of brain tumors using this method. Brain tumors are often deep in the brain, and open-skull surgeries are highly invasive and complex, making it challenging for conventional optical treatment procedures such as photothermal therapy, even during a single surgery session [7].

Here, we revisited the concept of photothermal therapy and developed a new remotely controlled approach for continuous and long-term photothermal therapy of the brain tumors in freely-behaving mice, without repeated open skull surgeries, and administration of anesthetic or analgesic drugs during the treatment sessions. This approach required integration of a wirelessly-powered light-emitting device that could be subcutaneously implanted on the skull to irradiate the nanoparticles in the tumor microenvironment. We tuned our devices to generate tissue-penetrating NIR light with different wavelengths and

intensities for efficient photothermal activation of the nanoparticles at any regions of interest in the brain. On the other hand, we developed gold nanostars with high absorption in NIR range and tuned their light absorption rate and photothermal efficacy to match the wireless signal transfer rate (*e.g.*, frequency and duty cycle) and optical power of our light-emitting devices. Gold nanostars have been extensively used for cancer imaging (*e.g.*, intraoperative Raman-guided tumor resection [6]) and photothermal tumor treatment [8], because of their facile synthesis and tunable optical properties [9,10]. We administered our nanostars intratumorally and wireless treatment was repeated for up to 15 days to treat three types of orthotopically-implanted brain tumors with minimal disturbance in normal activities of the animals during the treatment sessions. Our therapeutic approach was effective as evidenced by prolonged survival, histological analysis and electron microscopy of the tumor tissues. This is the first report of on-demand and continuous photothermal therapy in awake animals, promises less clinical translational hurdles and can be feasibly modified for different tumors.

Designing nanoparticles for wireless photothermal therapy

We used star-shaped gold nanoparticles as our photothermal agents (Figs. 1A-C), due to their effective surface plasmon characteristics in NIR range, biocompatibility, and facile synthesis and surface functionalization [6]. Our photothermal agents consisted of an active monolayer of Raman reporter molecules (BPE) and were coated with Cy5-labelled polyethylene glycol (PEG, MW ~ 5 kDa) molecules (Fig. 1A and Supplementary Fig. 1A). Nanoparticles were tagged with Cy5 and BPE molecules to enable their tracking within the tumors and their surrounding normal brain tissues using near-infrared fluorescent (NIRF) and Raman (SERS) imaging (Fig. 1J and Supplementary Figs. 2-5). Also, PEG molecules enhanced their stability in tumor microenvironment, enabling their selective diffusion in the tumors, due to their enhanced permeation and retention (EPR, Fig. 1J and Supplementary Fig. 6) [11]. Our fluorescent microscopy analysis (Supplementary Figs. 7) showed that intratumorally injected nanoparticles were mostly accumulated in tumors over the entire period of the treatment and we did not detect them in adjacent brain tissues. We also used inductively coupled plasma (ICP) to detect any traces of gold in different sections of the formalin-fixed brains (n=3 mouse) with a ppm detection accuracy, and did not detect noticeable amount of gold ions in areas other than the tumors at the end of survival period.

Designing wirelessly-powered near infrared emitting devices

Far-field (FF) [12-14], near-field (NF) [15-18], and mid-field (MF) [19,20] radiofrequency (RF) communication modalities have been utilized for wireless power delivery to a variety of light-emitting implantable bioelectronic devices. Since our nanoparticles required relatively higher optical irradiation power levels (tens of mWs) over shorter distances (*i.e.*, less than 1.5 cm in mouse brain), we used NF wireless power delivery to our devices [17]. Previously reported NFC [15-18] and MF [19-21] methods have been used to deliver lower optical powers (*e.g.*, ~1-5 mW) of shorter wavelengths (less than 700 nm) to tissues over a smaller distance (*i.e.*, less than 1 mm and adjacent tissues). However, our method was designed to generate higher optical powers (*e.g.*, ~ 25-50 mW) of longer wavelengths, which have higher tissue penetration rates (Supplementary Fig. 10) [22,23]. Therefore, this approach can target relatively

larger tumors (up to 3-5 mm^3, in brain depths of at least 0-5 mm depending on the wavelength), as also verified in our theoretical estimations (Supplementary Fig. 11). The irradiation area can also change with the beam shape, as well as optical power and number of the LEDs used in each device. The maximum treatable tumor size is also dependent on nanoparticles dosage and photothermal efficacy [4]. Higher dosages of the nanoparticles, or using nanoparticles with higher photothermal efficacy can generate more heat at lower optical powers (*i.e.*, deeper tumors) and help to treat larger tumors.

We selected 13.56 MHz (NFC band) for wireless power delivery, due to availability of different commercial products as well as significantly lower tissue absorption compared to higher frequency bands [19,20,24], allowing for safe transmission of such high power levels to the nanoparticles within the radiation safety guidelines [25]. Unlike our devices which were designed to send tissue-penetrating NIR (longer wavelengths) to the nanoparticles in deeper regions of the brain, all previously reported light-emitting implants were designed for applications other than activating nanoparticles, and had to be adhered to the targeted tissue [17,18] or inserted into the organ (*e.g.*, brain) directly [13,15], to ensure efficient light delivery, since visible light has a very limited tissue penetration [26]. The fabricated devices are shown in Figs. 2A-B and Supplementary Figs. 13 and 14. The final devices were coated with a 2-μm thick parylene-C layer (Fig. 2C and Supplementary Fig. 15) prior to implantation to prevent moisture diffusion and prolong their post-implantation lifetime [27,28].

Irradiating the nanostars with intermittent (duty-cycled) optical power is essential to maintain their morphological stability for long-term repeated photothermal therapy sessions (Supplementary Fig. 8). It also allowed for LED heat mitigation (Fig. 2D), which was necessary to ensure device safety after implantation. Duty-cycling could either be implemented using a switch on the implant with programmable timing capability or by modulating the incoming power signal (Figs. 2E and F). Alternatively, the inherent rectifying behavior of the LEDs could be used to implement duty-cycling, as shown in Fig. 2G, in which maximum theoretical duty cycle was 31.8%. This could be effectively doubled by employing two LEDs with reverse polarities (*i.e.*, back-to-back or BB design, Fig. 2H and Supplementary Fig. 16). The combined power of the two LEDs was equivalent to that of a single LED with 63.6% duty-cycle providing sufficient photothermal efficiency in the brain. Since each LED was on only half the time, self-heating was effectively mitigated. Moreover, the BB design improved the photothermal therapeutic efficacy, due to irradiating larger volumes of the tumors (Supplementary Fig. 11) and simultaneously, enhancing photothermal effect of the nanoparticles by absorbing larger number of photons [29]. BB design offered a lower component count, more simplicity, and a higher efficiency compared to the conventional design (Fig. 2F), in which RF-to-DC converters were needed (See Supplementary Text) [20,30]. Additionally, we evaluated the light-emitting efficacy of the BB devices by applying a sinusoidal input with different amplitudes and measuring the temperature of the nanoparticles using a thermal infrared (IR) camera. The results are shown in Fig. 2I for both 810-nm and 940-nm LEDs, suggesting that a peak voltage of ~4 V (P_{in} ~ 80 mW or 19 dBm) was required to produce sufficient photothermal effect within a nanoparticles' droplet (*i.e.*, 10 μL, $\Delta T > 3$ °C).

Balancing power transfer and photothermal effect in tumors

Our approach was designed based on a 3-step power transfer mechanism to activate nanoparticles photothermal effect in the brain of freely-behaving mice: (1) wireless power transfer from the transmitter (TX) coil to the antenna on the device; (2) conversion of electrical signals to NIR light with desired wavelength and optical power; and (3) NIR delivery to the nanoparticles in the brain tumors and their interaction to generate photothermal energy. Considering these three steps, we tuned electrical power transfer parameters and optical design of our setup to generate sufficient and long-term consistent photothermal heat from the nanoparticles in the tumors (*i.e.*, $\Delta T \sim 3\text{-}5$ °C), without heating side-effects on other parts of the body, due to wireless electromagnetic power transfer.

Since the input impedance of the BB LEDs is non-linear, we performed large-signal S-parameter (LSSP) simulations to evaluate the variations in matching network efficiency (η_{MN}) *vs.* P_{in} (Fig. 3C and Supplementary Fig. 19B; also see Section 2c of the Methods for details). These results indicated that although changes in device orientation or its distance from the TX coil could decrease η_{MN} from its optimum value, variations in P_{in} were limited to 2 dB (within the range required for delivering sufficient optical power to the tumor). This ensured consistent power transfer between the TX coil and implanted devices for consistent NIR irradiation of the nanoparticles and efficient photothermal therapy effects in freely-behaving mice.

Also, we simulated the specific absorption rate (SAR, units of W/kg) over the entire mouse body to ensure electromagnetic irradiation safety during our photothermal therapy sessions. SAR represents the rate of energy (RF electromagnetic waves) absorbed per unit mass of the tissues, and hence intrinsic tissue heating without any nanoparticles. In other words, SAR is a major safety criterion to determine the wireless power levels [25]. Fig. 3D and Supplementary Fig. 20 show 1-g SAR simulation results at 13.56 MHz (NFC frequency) and 915 MHz (a typical FF range, shown for comparison), using muscle model for the mouse. Unlike the absorption rate values obtained for 915 MHz, the 1-g SAR value at 13.56 MHz was below the maximum allowable value (1.6 W/kg), verifying that our wireless power transfer approach was safe according to Federal Communications Commission (FCC) regulations [25] (See Supplementary Text for details). Our full-wave simulation (Fig. 3E) showed that the power delivered to the LEDs was decreased about ~5 dB at 13.56 MHz, due to tissue interactions. However, this degradation did not decrease the NIR emission power of the devices and therefore, we could achieve the required photothermal therapy effect without any need to increase the nanoparticles dosage in the tumors. Moreover, our *in vivo* thermal imaging results (Fig. 3F and Supplementary Figs. 22-23) verified that tumor areas were the only site in the brain which showed elevated temperature, and this was entirely due to the photothermal interaction of nanoparticles with incoming NIR photons. We did not observe any temperature increase in surrounding normal brain tissue or other parts of the body during the treatment. All these adjustments together ensured, overall safety of our wireless power transfer approach, as well as precise and effective heating of the tumors in freely-behaving mice.

Photothermal therapy of brain tumors in freely-behaving mice

Human U87-eGFP-fLuc glioblastoma tumors were used for preliminary evaluation of our wireless photothermal therapy technique. *In vivo* thermal imaging showed that the nanoparticles' photothermal effect increased the tumor temperature to ~40.3°C (peak ΔT = 5.2 °C) during the irradiation with 810-nm wavelength (Figs. 3F-G and Supplementary Figs. 22-23). These results matched with the nanoparticles *in vitro* and *ex vivo* thermal imaging results (Figs. 1C, F and G), as well as the broad-band light absorption spectrum of these nanoparticles (Supplementary Fig. 1B).

Distance between the implanted device and the center of the TX coil could change spontaneously due to movements of the freely-behaving mouse in the therapeutic cage (Figs. 4A, B and D, and Supplementary Figs. 24-25, diameter ~ 13.5 cm), and this could possibly result in different optical powers delivered to the nanoparticles in tumors. Therefore, we measured optical power generated from each device at different points above the TX coil to evaluate these variations quantitatively (see experimental setup in Supplementary Fig. 26) and tuned the electrical parameters for consistent nanoparticles irradiation during the treatment cycles. The TX power levels were fixed at −10 dBm for the 940-nm device; however we observed lower output power (and therefore photothermal effect) than expected for the 810-nm device, requiring 1 dB higher power. This was due to the different geometrical shape and larger metal pads of our 810-nm LEDs that altered the antenna impedance (Supplementary Figs. 12A and 14). Two-dimensional variations of optical power delivered to nanoparticles at different heights (h) within the therapeutic cage are shown for both 810-nm and 940-nm devices in Fig. 4E and Supplementary Figs. 27-28. These measurements suggest that when h changed between 1 to 5 cm, the maximum variations in the received power levels were ~8 and 3 dB for the 810-nm and 940-nm devices, respectively. These maximum variations were observed at the largest h value (*i.e.*, h = 5 cm), where we had relatively lower electrical and optical power levels (Supplementary Fig. 29 and Fig. 4E). Larger optical powers and photothermal effects were observed at lower heights and maximum power and photothermal heating were achieved at h = 0 cm.

Additionally, in order to deliver sufficient and approximately similar amount of heat to the tumors for both 810- and 940 nm devices (see Supplementary text), and account for all possible movements of freely-behaving mice, probable misalignments between the TX and RX coils, and the loss inside the tissue (~ 5 dB, due to loading effects, as shown in Fig. 3E), a multi-level powering scheme was chosen, in which the TX power level was increased in three different steps all within FCC safety guidelines (Fig. 4C and Supplementary Fig. 30). Temperature profiles of the devices at these different power levels were also monitored using high-resolution thermal imaging (Fig. 2D and Supplementary Figs. 31-32).

Wireless photothermal therapy (15 min/day, repeated for 15 days) was started 24 h after intratumoral injection of nanoparticles and subcutaneous implantation of devices on the skull. Both types of devices (810-nm or 940-nm) were effective in photothermal treatment of U87 tumors and prolonging the survival of the mice, in comparison with control groups (Fig. 4F; See Supplementary Text for details of clinical translation perspective [2,31,32]). Treatment did not interfere with the mice normal activities and we did not observe any

side-effects or behavioral change due to wireless power transfer, NIR irradiation, presence of the nanoparticles in tumors, and photothermal heating of the tumors (Supplementary Video 1). We also compared our wireless therapeutic results with mice treated with a tethered photothermal therapy approach, in which microfibers (200 μm diameter, 2-3 mm length, Supplementary Figs. 35 and 36) were implanted for direct light delivery to nanoparticles in the tumors (Supplementary Figs. 37-40). The survival results and nanoparticles therapeutic effects were statistically similar in both wireless and tethered NIR light delivery approaches (Fig. 4F). Significantly prolonged survival was also observed in mice that were simultaneously treated with a daily dosage of temozolomide (TMZ, a common drug for GBM chemotherapy, Supplementary Fig. 41). This enhanced survival is promising as combination of different therapeutic modalities (*e.g.*, surgery, chemotherapy, and radiation therapy) is often preferred to achieve better GBM therapy outcomes in clinics. We also evaluated this technique using GL26 syngeneic mouse GBM cell line and infiltrating human-derived GBM39 [33,34] xenografts (in immunocompetent and athymic mice, respectively). All treatment parameters were similar to what we used for U87 tumors. We observed statistically significant improvement in survival of these mice (Supplementary Figs. 42-43).

Brains and nanoparticles embedded in tumors were analyzed by NIR fluorescent (NIRF) and Raman microscopy imaging, scanning electron microscopy (SEM), and histology (hematoxylin and eosin [H&E], and apoptosis markers) before and after treatments. Comparison of the NIRF, Raman, and H&E images (n=3) showed that nanoparticles only diffused into the tumor tissue within 1.5-2 mm rostral and caudal to the site of intratumoral injection (Figs. 1J-L and Supplementary Figs. 3-4). Note that NIR fluorescent and Raman signals were only generated from nanoparticles (see control data in Supplementary Fig. 5), without any signal interference from background tissue. The brightest regions of the NIR fluorescent and Raman images (sections 3 and 4 in Fig. 1J and Supplementary Figs. 3-4) represent the highest nanoparticles concentration at the injection site. Fluorescent microscopy of the brain tissues at the end of the survival period also verified that nanoparticles were mainly accumulated in tumors over the entire treatment process (Supplementary Fig. 7). Additionally, SEM analysis at the border between tumor and normal brain further confirmed the nanoparticles' selective diffusion and photothermal effect within tumor tissues. Fig. 4G(i) shows secondary electron image on a selected zone of the tumor tissue section (100-μm thickness) after photothermal effect of the nanoparticles. Fig. 4G(ii) shows higher magnification backscattered electron image of a zone selected from Fig. 4G(i). White spots in Fig. 4G(ii) show the distribution of nanoparticles in tissue, since gold generates a strong bright contrast in the SEM backscattered mode, which helped distinguishing them from the tissue that did not contain nanoparticles. The backscattered electron image in Fig. 4G(iv) also shows the nanoparticles (bright contrast) within the photothermally affected tumor region shown with arrows (compare with counterpart secondary electron image in Fig. 4G(ii)). H & E analyses of the tissues obtained from the mice at the end of treatments showed tumor necrosis, tumor cell death, shrinkage, and perturbation of the tumor microstructure consistently in U87, GL26, and GBM39 tumors as the result of photothermal effect of the nanoparticles (Supplementary Figs. 44-47). The untreated tumors were lacking areas of response ("R") and these specific necrosis patterns

("N") and were densely composed of cancer cells due to unimpeded proliferation (n=5 treated *vs.* control brains). We also noted considerable tumor apoptosis after a single day photothermal treatment (Supplementary Fig. 48), which indicates the relative effectivity of our method over short treatment periods. However, due to rapidly growing nature of the GBM, mice that were treated for shorter times (*i.e.*, 5 and 10 days treatment) had a significantly shorter survival compared to mice that were treated up to 15 days.

Conclusions

Current photothermal therapy approaches are not clinically efficient for treatment of brain tumors, since a complicated open skull surgery is needed to expose the tumor and irradiate the nanoparticles. This is even more challenging when tumors are seated in deep brain regions or beside major blood vessels. Here, we combined the state-of-the-art photothermal therapy with recent advancements in bioelectronics to resolve this major clinical challenge. Epidermal and implantable bioelectronics have been developed for diverse healthcare monitoring and therapeutic purposes, yet have not been investigated systematically for cancer therapy or diagnosis [35-37]. This is mainly because of nascent stages of bioelectronics development as an emerging technology, as well as biological complexity and anatomical diversity of different types of cancers, such as heterogeneities of tumor tissues and lack of easy access to deep tissue tumors [38]. To resolve these challenges, we designed an implantable and flexible bioelectronic platform to trigger nanoparticles photothermal therapeutic reactions in the brain tumors for on-demand and point-of-care treatment cycles. Our nanoparticles were designed to generate a uniform therapeutic action in the brain tumor microenvironment, when activated with our wirelessly powered light-emitting devices. Nanoparticles enabled precise treatment of the tumors without any noticeable heating effect on surrounding normal brain tissues. Daily treatments were pursued wirelessly, without any additional surgery or interrupting the normal activities of the mice. These results suggest the efficacy of our therapeutic method in clinical GBM therapy applications, especially when it is combined with standard therapeutic modalities such as chemotherapy, and radiation therapy, as well as investigational therapies such as immunotherapy (see perspectives and potential clinical impacts in Supplementary Text).

Methods

1. Synthesis and characterization of gold nanoparticles as photothermal agents

a) Synthesis.—Star-shape gold nanoparticles (nanostars) were synthesized following a method reported previously [6]. Purified nanostars solution was added to a mixture of Cy5-PEG(5kDa)-thiol (Nanocs, USA) and trans-1,2-bis (4-pyridyl)-ethylene (BPE, Sigma Aldrich, USA) and wrapped in aluminum foil, followed by gentle shaking at room temperature for 2 h. Thiol (−SH) terminating side of the PEG molecules reacted with gold surface and helped to stabilize the nanoparticles. Cy5 and BPE were included for tracking the nanoparticles in cancer tissues, due to their near-infrared fluorescent and surface enhanced Raman imaging signals. Final mixture was purified by centrifuging (2000 rcf for 10 min), removing the supernatant and re-dispersing the nanoparticles pellet in 5% dextrose

(D5W) solution for 3-5 times. The final concentration of the nanoparticles solution was adjusted to 0.5 nM.

b) Characterizations.—Dynamic light scattering (DLS, Malvern, USA) was used for measuring the hydrodynamic size of the nanoparticles. Transmission electron microscopy (TEM, 200 kV, FEI Tecnai, USA) was used for morphological analysis of the final nanoparticles. UV-vis (Agilent Cary 6000i UV/Vis/NIR, USA) was used to determine the absorption spectrum of the nanoparticles. Absorption values measured by Thermo Scientific NanoDrop spectrophotometer (USA) and inductively coupled plasma mass spectroscopy (ICP-MS, Thermo Scientific XSERIES 2, USA) were used to determine the nanoparticles concentration. Surface enhanced Raman spectrum of the nanoparticles was determined using an InVia Renishaw Raman microscope (USA). Finally, photothermal heating efficacy of the nanostars in response to NIR irradiation was investigated using the thermal camera.

2. Fabrication and electro-optical characterization of NIR-emitting devices to trigger nanoparticles photothermal effect

a) DC characterization of LEDs.—LEDs emitting 810 nm and 940 nm NIR lights were purchased from Shenzhen Best LED Opto-Electronic Co. (2835FIRC-81L, China) and Vishay Semiconductors (VSMY14940, Germany), respectively. A DC power supply (E3631A, Agilent, USA) was used to characterize LED efficiencies, and the minimum power required for heating the nanoparticles up to a specific temperature (*e.g.*, $\Delta T = 3$ °C). A pair of 34-gauge enameled wires were soldered onto the two terminals of each LED, which were then connected to the power supply to determine their current-voltage characteristics. The LEDs were fixed on an optical sensor (S130C, Thorlabs, USA) to measure their electrical-to-optical conversion efficiency, η. Optical power was measured using an optical power meter (PM100D console, Thorlabs, USA). This process was repeated for both LEDs used in this study. Next, LED temperatures and the nanoparticles' heating effect were measured. LEDs were fixed at 2 mm away from a droplet of nanoparticles, and a thermal camera (A8201sc InSb, FLIR Systems, USA) was placed at ~10 cm above them to measure heating effects.

b) Characterization of the back-to-back design of LEDs.—Two LEDs were soldered with reversed polarity (Figs. 2A and H) to characterize the efficacy of the back-to-back LED design. First, LEDs were placed at 2 mm from the nanoparticles. Then, we used an arbitrary waveform generator (4052, BK Precision, USA) to generate a sine wave. The waveform generator was used in High-Z mode and the amplitude was swept while the nanoparticles' temperature was measured. Nanoparticles and LED temperatures were both recorded for further analysis (Supplementary Fig. 31). The power conversion efficiency (PCE) of the back-to-back topology was calculated using harmonic balance simulation in ADS simulator (Keysight, USA) (Supplementary Fig. 17, also see Supplementary Text). We used the electrical characteristics provided by the vendors to build a simulation model. Similarly, we simulated the conventional circuit topology for wireless powering of the LEDs (Fig. 2F), which included a matching network, a rectifier, and an energy storage capacitor (1 μF). The definition and values of different power efficiency parameters of our devices are provided in Supplementary Text. Moreover, we determined variations of duty-cycle,

average power, and equivalent DC power (P_{dc}) with amplitude of the applied voltage for back-to-back and single LED designs for comparison (Supplementary Fig. 18).

c) Back-to-back LED RF characterization and matching for maximum power delivery and sufficient photothermal efficacy.—The impedance profile of the back-to-back LEDs were characterized at 13.56 MHz to find the matching component values. The impedance of a LED is non-linear as its resistive and capacitive components vary with the input power level. Therefore, we characterized the impedance at the power levels of interest. The S_{11} for each case was recorded using a vector network analyzer (VNA, E5072A, Agilent, USA) with input power in range of 14-20 dBm with steps of 1 dB. We developed a circuit model based on these measurement results. The simulated results were in close agreement with measured data as shown in Fig. 3A and Supplementary Fig. 19. These models were used for further simulations, such as those used to evaluate the effect of input power fluctuations shown in Fig. 3C. The commercially available NFC antenna was characterized using the VNA by soldering an SMA connector and recording the S_{11} data for post-processing.

(d) Device fabrication.—The LEDs were put in place and soldered to the capacitors (matching components) and the antenna using two pieces of short 34-gauge enameled wires (Fig. 2A). Three versions of the devices were prepared consisting of two 940-nm LEDs, two 810-nm LEDs, or integrating one 940-nm and one 810-nm LED (hybrid devices), as shown in Supplementary Fig. 14. The whole structure was glued using Vetbond tissue adhesive (3M, USA) to form a transparent and thin supporting layer around the LED, wires, and matching capacitors. Next, parylene C was deposited using an SCS Labcoater 2 (Specialty Coating Systems Inc., USA) to a thickness of 2 μm. 3-(trimethoxysilyl) propyl methacrylate (A-174 Silane) was used as an adhesion promoter to maximize the adhesion of the parylene film to the surface of the devices. Scanning electron microscopy (SEM, FEI Magellan, USA) was used to evaluate parylene deposition (Fig. 2C and Supplementary Fig. 15). Fig. 2B and Supplementary Fig. 14 show the fabricated wireless implant.

e) Evaluating wireless NIR-emission efficiency of the devices.—An external loop antenna (Antenna Coil 12.3 cm, Emma Technology, China) was characterized and matched at 13.56 MHz, and then used as the transmitter (TX) coil in our wireless setup. The antenna diameter was 12.3 cm which matched the dimension of the therapeutic chamber (13.5 cm, Figs. 4B and D). The excitation signal was generated by a signal generator (N9310A, Keysight, USA, Fig. 4A) and then amplified using a power amplifier (PA, LZY-22+, Minicircuits, USA). The PA output power level was determined by assessment of three factors, namely the nanoparticles' photothermal effect, LED electro-optical efficiency, and radiation safety concerns. The efficacy of the selected power levels (−9 dBm for 810-nm LEDs and −10 dBm for 940-nm LEDs) was evaluated by measuring the optical power emitted from LEDs, when the devices were placed at different locations inside the therapeutic chamber (setup shown in Supplementary Fig. 26). As shown in this schematic, the LEDs were not placed directly on the optical power sensor. This was because the body of the optical power sensor was composed of metal parts and placing the receiver antenna (the whole NIR-emitting device) directly on top of it could result in cancellation of the RF signal.

Instead, the antenna was connected to the LEDs through a pair of 34-gauge enameled wires and the LEDs were placed on the power sensor, while the antenna was moved to different locations within the RX coil to evaluate the electro-optical efficiency. At each point, the optical power generated by the LED was measured using the optical power meter and the location of the antenna was recorded using a polar coordinate paper placed on top of the TX coil. Nominal power levels were used for all measurements. MATLAB (Mathworks, Natick, USA) was used to create the optical power maps at different heights for each device (Fig. 4E and Supplementary Figs. 27 and 28). We employed a multi-level powering scheme (Supplementary Fig. 30) to account for the loss due to implantation (tissue effect) and possible orientation and distance variations between the device (RX) and TX coil. To ensure device heating is not an issue, each device was placed in the middle of the TX coil at h = 0 cm for maximum power transfer and maximal heating and device temperature was recorded in all power levels. For this measurement, the coil was connected to the PA and the PA was connected to the signal generator (DS1104Z Digital Oscilloscope, RIGOL, China) and the output RF power of the signal generator was set according to the steps shown in Supplementary Figs. 24 and 30. The thermal camera was placed at a distance of 10 cm from the devices (Supplementary Fig. 31) and thermal images of the LEDs were measured.

f) Mouse SAR simulation to evaluate safety of the wireless electromagnetic power transfer during the photothermal treatments.—We used simulation to evaluate specific absorption rate (SAR) in the mouse body, in order to assess possible tissue heating during the wireless photothermal therapy sessions. The simulation was done at 13.56 MHz and the highest TX power level (−4 dBm), to calculate 1-g SAR (SAR averaged over 1 g mass of tissue in the shape of a cube per FCC regulation) in a 3D full-wave simulator (CST Studio Suite, Simulia, France) using the finite element method and a 3D mouse model. In this simulation, the mouse was placed in the middle of a two-turn coil (copper) to model the transmitter coil, and on top of a FR-4 board. Mouse body was modelled as muscle (with blood flow) with permittivity of $\epsilon = 66 - j127$ and $\epsilon = 55 - j18$ at 13.56 MHz and 915 MHz (for comparison), respectively. CST's internal post-processing SAR tool was used after a frequency domain simulation with tetrahedral mesh type and a lumped port. The dimensions of the mouse model in this simulation were 2.2 cm × 10.5 cm × 3.4 cm (W × L × H).

3. Tumor models

a) Animal models: Athymic CD-1 nude mice (25-30 g, 10 weeks old, female, Charles River Laboratories, USA) and immunocompetent C57BL/6J mice (20-25g, 8 weeks old, female, Jackson Laboratory, USA) were used as models for our studies, following the animal use protocols reviewed and approved by the Institutional Animal Care and Use Committee (IACUC) at Stanford University.

b) Orthotropic brain tumor implantation: U87-eGFP-fLuc (gift from Dr. Irina V. Balyasnikova at Northwestern University) and GBM39-fLuc human glioblastoma cells (gift from Dr. Paul Mischel at Stanford University, ~2.4×10^5 cells in total volume of 3 μL phosphate buffered saline solution) were stereotactically injected at 0.5 mm posterior and 2.0 mm lateral to the bregma (at 3 mm depth) of the CD-1 mice (n = 95 mice for U87 and n = 20 mice for GBM39). U87 and GBM39 cells were cultured according to our previously

reported study [34]. Syngeneic mouse GBM cells (GL 26-fLuc, gift from Dr. Gerald Grant at Stanford University, ~10^5 cells in total volume of 3 μL phosphate buffered saline solution) were also cultured and injected at the same brain coordinates in immunocompetent mice (n = 20) using a previously reported method [39]. These cells were modified to express eGFP and firefly luciferase (fLuc) for fluorescent and bioluminescent imaging, respectively.

c) Monitoring the tumor size and shape: Our cells were modified to express luciferase, which enabled estimation of tumor size and morphology using bioluminescent and fluorescent imaging, in addition to T1-weighted MRI (pre- and post-gadolinium contrast injection). Tumor size was routinely evaluated using bioluminescence imaging (BLI, IVIS Spectrum, Xenogen Corporation, USA) and Living Image software. D-Luciferin (30 mg/mL, 150 mg/kg dose) was injected intraperitoneally and mice were imaged to assess the brain tumor burden by comparing the BLI signal intensities. Shape and growth pattern of the tumors were determined using T1-weighted magnetic resonance imaging (MRI, 3T, MR Solutions, USA). 6 μL of a clinical grade gadolinium based contrast agent (Multihance, USA) was mixed with 94 μL of PBS and the mixture was administered intraperitoneally. Pre- and post-Multihance T1-weighted brain MRI scans were performed with 1 mm slice thickness. MRI results were analyzed using OsiriX software.

4. Intratumoral administration of the nanoparticles for photothermal therapy

Nanoparticles (1 μL, 0.5 nM) were stereotactically injected into tumors, when post-Gd T1-weighted MRI analysis confirmed that the tumor size reached to a contrast-enhancing volume of ~ 3 mm^3 (~2-3 weeks after implantation of the tumors), using a low speed micro-pump (injection rate ~ 0.5 μL/min, Pump 11 Elite Nanomite, Harvard Apparatus, USA) and a Hamilton syringe. The needle was pulled out gently (1 mm/min), followed by immediate sealing of the skull hole using bone wax and suturing. Step-by-step injection was used to avoid leakback of the nanoparticles as the result of tumors hydrodynamic pressure. For example, for injecting the nanoparticles at a depth of ~ 3 mm, we first inserted the needle to coordinate its tip at 4 mm depth. Then, we pulled out the needle tip to the depth of 3 mm after 1 min waiting, followed by injecting 0.5 μL of the nanoparticles (0.5 μL/min). Then, the micro-pump was stopped and the needle was pulled out for another 1 mm after 1 min, and the rest of the nanoparticles were injected. The needle was pulled out 1 mm after 1 min waiting and this process continued until the needle tip was completely out, immediately followed by sealing the hole using bone wax. This step-by-step pulling out and slow injection approach enabled us to deposit the nanoparticles solution into the empty spaces generated by the needle. Control mice were injected with PBS (1×) using a similar method. Photothermal therapy sessions were started 24 h after administration of the nanoparticles.

5. Photothermal therapy of the brain tumors in freely-behaving mice

NIR-emitting devices were fixed on the skull using dental cement. Before this step micro-drilling was used for thinning the skull in a rectangular area under the location of LEDs for more efficient optical transparency and NIR delivery to tumors. For U87 tumor studies, three groups of mice were generated to evaluate the efficacy of our wireless photothermal therapy approach (n=10/group). Two groups of mice were injected with nanostars and

implanted with 810-nm or 940-nm NIR-emitting devices for photothermal treatment [NPs (+), 810-nm Device (+), Irradiation (+); NPs (+), 940-nm Device (+), Irradiation (+)]. One additional group of mice was investigated as control after injection of the nanostars and implantation of the devices, but without any irradiation for photothermal effects [NPs (+), Device (+), Irradiation (−)]. The results were compared with mice without any nanostars injection and device implantation [NPs (−), Implantation (−)]. Treatments started 24 h after intratumoral administration of the nanostars and each mouse was treated wirelessly in the therapeutic chamber for 15 min per day during the whole survival evaluation period. To ensure consistent tumor irradiation during the free movements of the mice inside the therapeutic chamber, multi-level powering was used, in which the power level transmitted to the implanted devices was increased in three different steps, as shown in Supplementary Fig. 30 (see details in Supplementary Text). A Python script was used to calculate the required voltage levels and communicated the information to a signal generator (RIGOL DS1104Z Digital Oscilloscope, China, the signal source for the *in vivo* experiments), using National Instruments' implementation of the Virtual Instrument Software Architecture API (NI-VISA) through a graphical user interface (GUI). This script set the required frequency (13.56 MHz) and output mode (50 Ω) and allowed users to select power levels and their duration for *in vivo* photothermal therapy sessions (Supplementary Fig. 24).

We also used a tethered light delivery approach to be compared with our wireless photothermal therapy approach. Microfibers (diameter~ 200 μm and lengths ~ 2-3 mm) passed through ceramic cannulas (Thorlabs, US) were implanted in the brain to guide the NIR light to tumors. Exact anatomical location of the tumors were first determined using post-Gd T1-weighted MRI. Micro-drilling was used to create a sub-millimeter sized hole in the skull overlying the center of tumors. The microfiber orientation and length was determined based on MRI assessment of the tumors for most efficient light delivery to tumors. Microfibers were implanted in the brain using a cannula implant guide and a stereotaxic cannula holder (OGL and XCL, respectively, Thorlabs, USA) after intratumoral administration of the nanostars, and dental cement was used to fix them on the skull. Incisions were closed using veterinary glue and mice were allowed to recover for subsequent photothermal treatments. Before each treatment session, mice were restrained for connecting the cannulas to optical fibers that were attached to laser sources (LP785-SF100, 785 nm, 100 mW, SM Fiber-Pigtailed Laser Diode, FC/PC, powered by an ITC4020 combined laser diode and thermo-electric cooler controller, Thorlabs, USA). The optical setups are shown in Supplementary Figs. 35 and 36. Treatments were performed on freely-behaving mice [treatment group: NPs (+), Microfiber (+), Irradiation (+) *versus* controls: NPs (+), Microfiber (+), Irradiation (−); n=10 per group, total=60 mice] using 785 nm irradiation (20 mW, 24 h after administration of nanostars, 15 min/day). For combination therapy studies, temozolomide (66 mg TMZ/kg suspended in Ora-Plus, Selleck Chemical LLC, USA) was administered *via* oral gavage for 5 consecutive days to mice with and without wireless photothermal therapy (*i.e.*, Days 1 to 5 after device implantation). Mice were euthanized when they lost 15% of the body weight and these end points were recorded to generate Kaplan-Meier plots. Similar wireless photothermal therapy experiments were used for nude mice with human GBM39 and immunocompetent mice with syngeneic GL26 tumors and survival results were compared. A calibrated thermal camera was used for *in vivo* and

ex vivo monitoring of the photothermal temperature changes in the tumors during NIR irradiations.

6. Analysis of the mouse brain tissues to evaluate nanoparticles photothermal effects

Mouse brains were excised and immediately imaged to evaluate near-infrared fluorescent (NIRF) signals originated from the nanoparticles, using the IVIS Spectrum system (excitation and emissions of 640 and 680 nm). For sectioning, brains were first fixed in 10% formalin and then stored in 30% sucrose solution for 3 days. Cryopreserved brains were then carefully embedded with known orientations in optimal cutting temperature (OCT) compound, followed by frozen sectioning (coronal, rostral to caudal) using a cryostat. At least N=6 adjacent 10- and 100-μm thick sections with a determined interslice gap (*e.g.*, 500 μm) were collected from the tumor region. 10-μm thick sections were stained using hematoxylin and eosin (H & E) for histology and determination of the tumor areas using Nanozoomer (NanoZoomer 2.0-RS whole slide imager, and NanoZoomer Digital Pathology (NDP) Scan version 2.5 software, Hamamatsu Photonics, Japan). Click-iTTM Plus TUNEL assay (Alexa FluorTM 594, Invitrogen, USA) of the paraffin-embedded and sectioned tissues was also used to detect early stage tumor apoptosis as a result of short-term photothermal therapy according to manufacturer's protocol. 100-μm thick sections were placed on quartz (Ted Pella Inc., USA) microscope slides for fluorescent and Raman microscopies. Quartz slides were used because of the high background Raman signal of the commonly used glass cover slides. An Odyssey scanner (700-nm channel with excitation and emission wavelengths of 685 nm and 705 nm, 20-μm resolution, LI-COR, USA) was also used for NIRF imaging of these tissue sections to determine distribution of the nanoparticles in tumors. Raman microscopy of these sections was also performed with dimensions covering the whole brain sections using the method we reported before [11]. NIRF and Raman images were compared to co-localize the multimodal signals originated from the nanoparticles and verify the distribution of the nanoparticles in the tumors. Finally, these sections were coated with a thin layer of AuPd to increase their conductivity and scanning electron microscopy was used for high resolution analysis of the nanoparticles in treated tumors using secondary electron and backscattered electron imaging. ICP samples obtained from different parts of the excised brains were also prepared and gold ions in tissue parts were estimated according to previously reported methods [11,40].

7. Statistics and reproducibility

All graph bars represent mean±s.d. and their statistical analyses were performed using two-sided student's t-test (Graphpad Prism). Logrank test was performed to compare the survival distributions in the animal studies (Stata/MP version 16.1). Comparisons with p-values less than 0.05 were considered to be statistically significant. All micrographs are representative of at least three independent experiments. All experiments were repeated at least three times with similar results.

Supplementary Material

Refer to Web version on PubMed Central for supplementary material.

Acknowledgements:

We acknowledge supports from Center for Cancer Nanotechnology Excellence and Translation at NCI-NIH (grant no. 1U54CA199075) and the NIH grants (NCI 1R01CA199656-01A1 and 1R01 CA222836-01A1). H. Arami was supported by NIH National Cancer Institute K99/R00 Pathway to Independence award (grant No.# 1K99CA234208-01A1) and NIH T32 CA009695 (Stanford Cancer Imaging Training, SCIT). L. Khalifehzadeh acknowledges the supports from NIH National Institute of Biomedical Imaging and Bioengineering (NIBIB) K99/R00 Pathway to Independence award (grant No.# 1K99EB031178-01) and NIH T32 CA196585 (Cancer-Translational Nanotechnology Training, Cancer-TNT) at Stanford University. CBP is a McNair Scholar supported by the McNair Medical Institute at The Robert and Janice McNair Foundation. A. Poon is a Chan Zuckerberg Biohub investigator. We thank Prof. Irina V. Balyasnikova at Northwestern University, and Dr. Marc D. Ferro at Stanford University for providing U87-GFP-Fluc cells, and helps for parylene coating, respectively. Additionally, we acknowledge CST for providing access to the 3D full-wave simulator (CST Studio Suite, Simulia, France). We also thank supports and guidance from Drs. Jianghong Rao and Heike Daldrup-Link at Stanford Department of Radiology that enabled us to complete this study. This paper is dedicated to Dr. Sanjiv Sam Gambhir, who we lost to cancer during the preparation of this manuscript.

Data availability:

The data supporting the findings of this study are available within the paper and its Supplementary Information files and are available from the corresponding authors upon reasonable request.

Code availability:

The custom script prepared for wireless photothermal therapy in this study is available to download from https://osf.io/5vqxc/

References:

1. Ostrom QT et al. CBTRUS Statistical Report: Primary Brain and Other Central Nervous System Tumors Diagnosed in the United States in 2013-2017. Neuro Oncol 22, iv1–iv96, doi:10.1093/neuonc/noaa200 (2020). [PubMed: 33123732]
2. Stupp R et al. Effect of Tumor-Treating Fields Plus Maintenance Temozolomide vs Maintenance Temozolomide Alone on Survival in Patients With Glioblastoma: A Randomized Clinical Trial. JAMA 318, 2306–2316, doi:10.1001/jama.2017.18718 (2017). [PubMed: 29260225]
3. Kok HP et al. Heating technology for malignant tumors: a review. Int J Hyperthermia 37, 711–741, doi:10.1080/02656736.2020.1779357 (2020). [PubMed: 32579419]
4. Bastiancich C, Da Silva A & Esteve MA Photothermal Therapy for the Treatment of Glioblastoma: Potential and Preclinical Challenges. Front Oncol 10, 610356, doi:10.3389/fonc.2020.610356 (2020). [PubMed: 33520720]
5. Pinto A & Pocard M Photodynamic therapy and photothermal therapy for the treatment of peritoneal metastasis: a systematic review. Pleura Peritoneum 3, 20180124, doi:10.1515/pp-2018-0124 (2018). [PubMed: 30911668]
6. Wei Q et al. Intraoperative Assessment and Photothermal Ablation of the Tumor Margins Using Gold Nanoparticles. Advanced Science 8, 2002788 (2021). [PubMed: 33717843]
7. Pinel S, Thomas N, Boura C & Barberi-Heyob M Approaches to physical stimulation of metallic nanoparticles for glioblastoma treatment. Adv Drug Deliv Rev 138, 344–357, doi:10.1016/j.addr.2018.10.013 (2019). [PubMed: 30414495]
8. Vines JB, Yoon JH, Ryu NE, Lim DJ & Park H Gold Nanoparticles for Photothermal Cancer Therapy. Front Chem 7, 167, doi:10.3389/fchem.2019.00167 (2019). [PubMed: 31024882]
9. Chatterjee H, Rahman DS, Sengupta M & Ghosh SK Gold Nanostars in Plasmonic Photothermal Therapy: The Role of Tip Heads in the Thermoplasmonic Landscape. Journal of Physical Chemistry C 122, 13082–13094 (2018).

10. Vo-Dinh T et al. Shining Gold Nanostars: From Cancer Diagnostics to Photothermal Treatment and Immunotherapy. Journal of Immunological Sciences 2, 1–8 (2018).
11. Arami H et al. Nanomedicine for Spontaneous Brain Tumors: A Companion Clinical Trial. ACS Nano 13, 2858–2869, doi:10.1021/acsnano.8b04406 (2019). [PubMed: 30714717]
12. Kim TI et al. Injectable, cellular-scale optoelectronics with applications for wireless optogenetics. Science 340, 211–216, doi:10.1126/science.1232437 (2013). [PubMed: 23580530]
13. Montgomery KL et al. Wirelessly powered, fully internal optogenetics for brain, spinal and peripheral circuits in mice. Nat Methods 12, 969–974, doi:10.1038/nmeth.3536 (2015). [PubMed: 26280330]
14. Park SI et al. Soft, stretchable, fully implantable miniaturized optoelectronic systems for wireless optogenetics. Nat Biotechnol 33, 1280–1286, doi:10.1038/nbt.3415 (2015). [PubMed: 26551059]
15. Kang SK et al. Bioresorbable silicon electronic sensors for the brain. Nature 530, 71–76, doi:10.1038/nature16492 (2016). [PubMed: 26779949]
16. Chung HU et al. Binodal, wireless epidermal electronic systems with in-sensor analytics for neonatal intensive care. Science 363, doi:10.1126/science.aau0780 (2019).
17. Lee Y & Kim DH Wireless metronomic photodynamic therapy. Nat Biomed Eng 3, 5–6, doi:10.1038/s41551-018-0341-8 (2019). [PubMed: 30932069]
18. Yamagishi K et al. Tissue-adhesive wirelessly powered optoelectronic device for metronomic photodynamic cancer therapy. Nat Biomed Eng 3, 27–36, doi:10.1038/s41551-018-0261-7 (2019). [PubMed: 30932063]
19. Agrawal DR et al. Conformal phased surfaces for wireless powering of bioelectronic microdevices. Nat Biomed Eng 1, doi:10.1038/s41551-017-0043 (2017).
20. Bansal A, Yang F, Xi T, Zhang Y & Ho JS In vivo wireless photonic photodynamic therapy. Proc Natl Acad Sci U S A 115, 1469–1474, doi:10.1073/pnas.1717552115 (2018). [PubMed: 29378941]
21. Ho JS et al. Self-tracking energy transfer for neural stimulation in untethered mice. Physical Review Applied 4, 024001 (2015).
22. Wang M, Kim M, Xia F & Xu C Impact of the emission wavelengths on in vivo multiphoton imaging of mouse brains. Biomed Opt Express 10, 1905–1918, doi:10.1364/BOE.10.001905 (2019). [PubMed: 31061766]
23. Stujenske JM, Spellman T & Gordon JA Modeling the Spatiotemporal Dynamics of Light and Heat Propagation for In Vivo Optogenetics. Cell Rep 12, 525–534, doi:10.1016/j.celrep.2015.06.036 (2015). [PubMed: 26166563]
24. Lee PM, Tian X & Ho JS in IEEE Biomedical Circuits and Systems Conference (BioCAS). 1–4.
25. U.S. FCC, 47 CFR 1.1310, Radiofrequency radiation exposure limits. Federal Communications Commission, Washington, DC.
26. Ash C, Dubec M, Donne K & Bashford T Effect of wavelength and beam width on penetration in light-tissue interaction using computational methods. Lasers Med Sci 32, 1909–1918, doi:10.1007/s10103-017-2317-4 (2017). [PubMed: 28900751]
27. Gutruf P et al. Wireless, battery-free, fully implantable multimodal and multisite pacemakers for applications in small animal models. Nat Commun 10, 5742, doi:10.1038/s41467-019-13637-w (2019). [PubMed: 31848334]
28. Shin G et al. Flexible Near-Field Wireless Optoelectronics as Subdermal Implants for Broad Applications in Optogenetics. Neuron 93, 509–521 e503, doi:10.1016/j.neuron.2016.12.031 (2017). [PubMed: 28132830]
29. Kim A et al. An Implantable Ultrasonically-Powered Micro-Light-Source (microLight) for Photodynamic Therapy. Sci Rep 9, 1395, doi:10.1038/s41598-019-38554-2 (2019). [PubMed: 30718792]
30. Tajima K et al. Wireless optogenetics protects against obesity via stimulation of non-canonical fat thermogenesis. Nat Commun 11, 1730, doi:10.1038/s41467-020-15589-y (2020). [PubMed: 32265443]
31. Holland JM, Mitchell TJ, Gipson LC & Whitaker MS Survival and cause of death in aging germfree athymic nude and normal inbred C3Hf/He mice. J Natl Cancer Inst 61, 1357–1361, doi:10.1093/jnci/61.5.1357 (1978). [PubMed: 280717]

32. Simpson JR et al. Influence of location and extent of surgical resection on survival of patients with glioblastoma multiforme: results of three consecutive Radiation Therapy Oncology Group (RTOG) clinical trials. Int J Radiat Oncol Biol Phys 26, 239–244, doi:10.1016/0360-3016(93)90203-8 (1993). [PubMed: 8387988]
33. Hettie KS, Teraphongphom NT, Ertsey RD, Rosenthal EL & Chin FT Targeting intracranial patient-derived glioblastoma (GBM) with a NIR-I fluorescent immunoconjugate for facilitating its image-guided resection. RSC Adv 10, 42413–42422, doi:10.1039/d0ra07245a (2020). [PubMed: 33391732]
34. Chang E et al. AshwaMAX and Withaferin A inhibits gliomas in cellular and murine orthotopic models. J Neurooncol 126, 253–264, doi:10.1007/s11060-015-1972-1 (2016). [PubMed: 26650066]
35. Won SM, Song E, Reeder JT & Rogers JA Emerging Modalities and Implantable Technologies for Neuromodulation. Cell 181, 115–135, doi:10.1016/j.cell.2020.02.054 (2020). [PubMed: 32220309]
36. Kim J, Campbell AS, de Avila BE & Wang J Wearable biosensors for healthcare monitoring. Nat Biotechnol 37, 389–406, doi:10.1038/s41587-019-0045-y (2019). [PubMed: 30804534]
37. Yang JC et al. Electronic Skin: Recent Progress and Future Prospects for Skin-Attachable Devices for Health Monitoring, Robotics, and Prosthetics. Adv Mater 31, e1904765, doi:10.1002/adma.201904765 (2019). [PubMed: 31538370]
38. Pucci C, Martinelli C & Ciofani G Innovative approaches for cancer treatment: current perspectives and new challenges. Ecancermedicalscience 13, 961, doi:10.3332/ecancer.2019.961 (2019). [PubMed: 31537986]
39. Murty S et al. Intravital imaging reveals synergistic effect of CAR T-cells and radiation therapy in a preclinical immunocompetent glioblastoma model. Oncoimmunology 9, 1757360, doi:10.1080/2162402X.2020.1757360 (2020). [PubMed: 32923113]
40. Tavares AJ et al. Effect of removing Kupffer cells on nanoparticle tumor delivery. Proc Natl Acad Sci U S A 114, E10871–E10880, doi:10.1073/pnas.1713390114 (2017). [PubMed: 29208719]

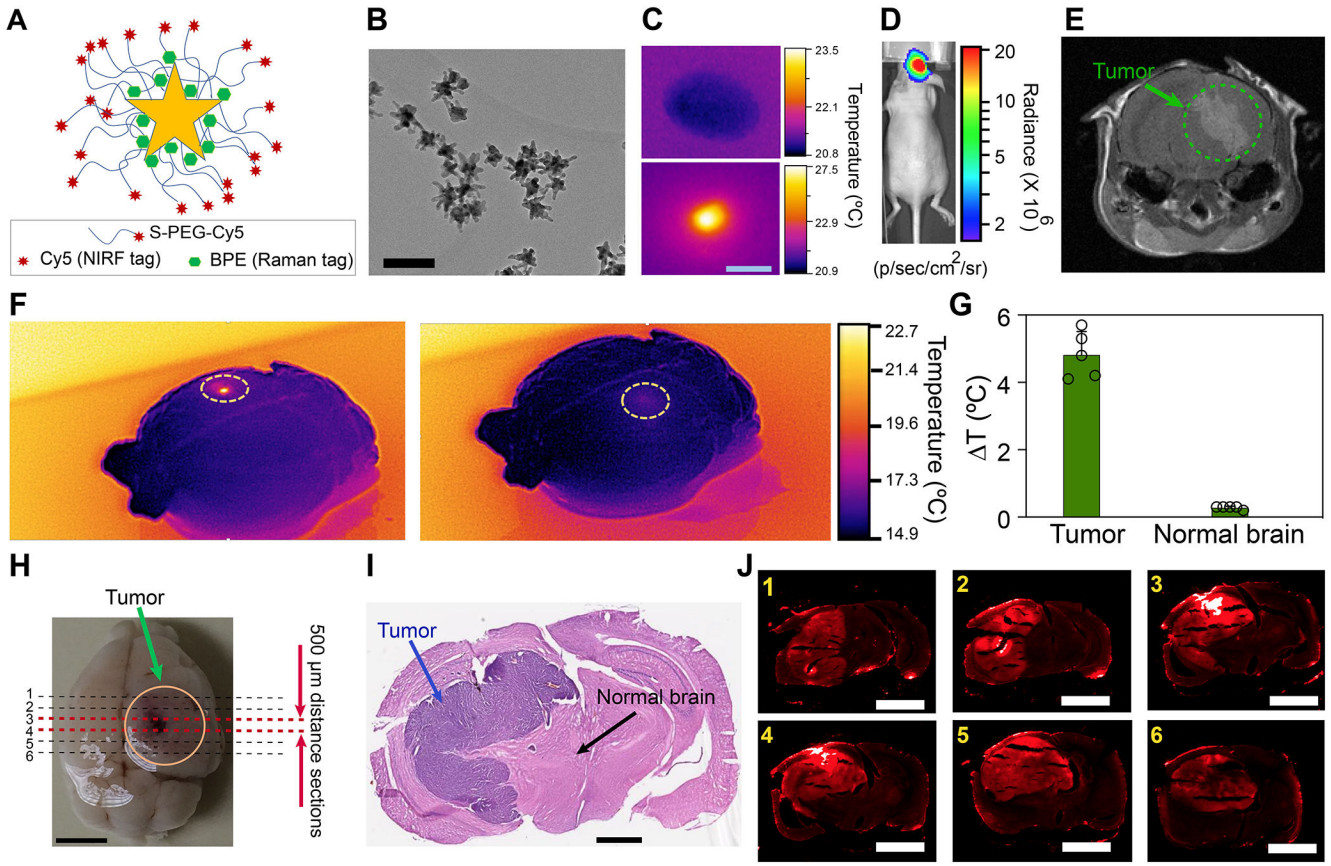

Fig. 1. Nanoparticles design for photothermal heating of the brain tumors.

(**A**) Schematic showing chemical conjugation of Cy5-labelled polyethylene glycol (Cy5-PEG) to the surface of nanoparticles tagged with BPE Raman reporter molecules. (**B**) Transmission electron microscopy demonstrating the star-shaped morphology of the nanoparticles for efficient photothermal heating in NIR range (scale bar: 100 nm). (**C**) Thermal image showing photothermal response of the nanoparticles under NIR irradiation (scale bar: 2 mm). (**D** and **E**) Bioluminescent imaging and T1-weighted MRI (post-Gd contrast) used to estimate tumor size (human U87-eGFP-fLuc glioblastoma) prior to injection of nanoparticles. (**F**) Thermal images of an excised brain. NIR-triggered heating was only observed in tumor areas injected with nanoparticles (left), without any noticeable heating effect in normal brain areas (right). (**G**) Quantitative analysis of the thermal images showed significant difference in temperature variation within the tumor and normal brain areas (mean±s.d., n= 5, two-sided student's t-test, p = 0.0001). (**H**) Photograph of an excised brain showing sectioning locations in the tumor areas to collect 6 consecutive brain slices for histology and fluorescent microscopy analysis (scale bar: 2 mm). (**I**) Histological analysis of an H&E stained tissue slice showing the tumor areas (scale bar: 1 mm). (**J**) Fluorescent imaging of the brain slices prepared in (H) (scale bars: 2 mm). Comparisons with counterpart histological analysis tissues verified that nanoparticles were only diffused into tumors (see control image in Supplementary Fig. 5).

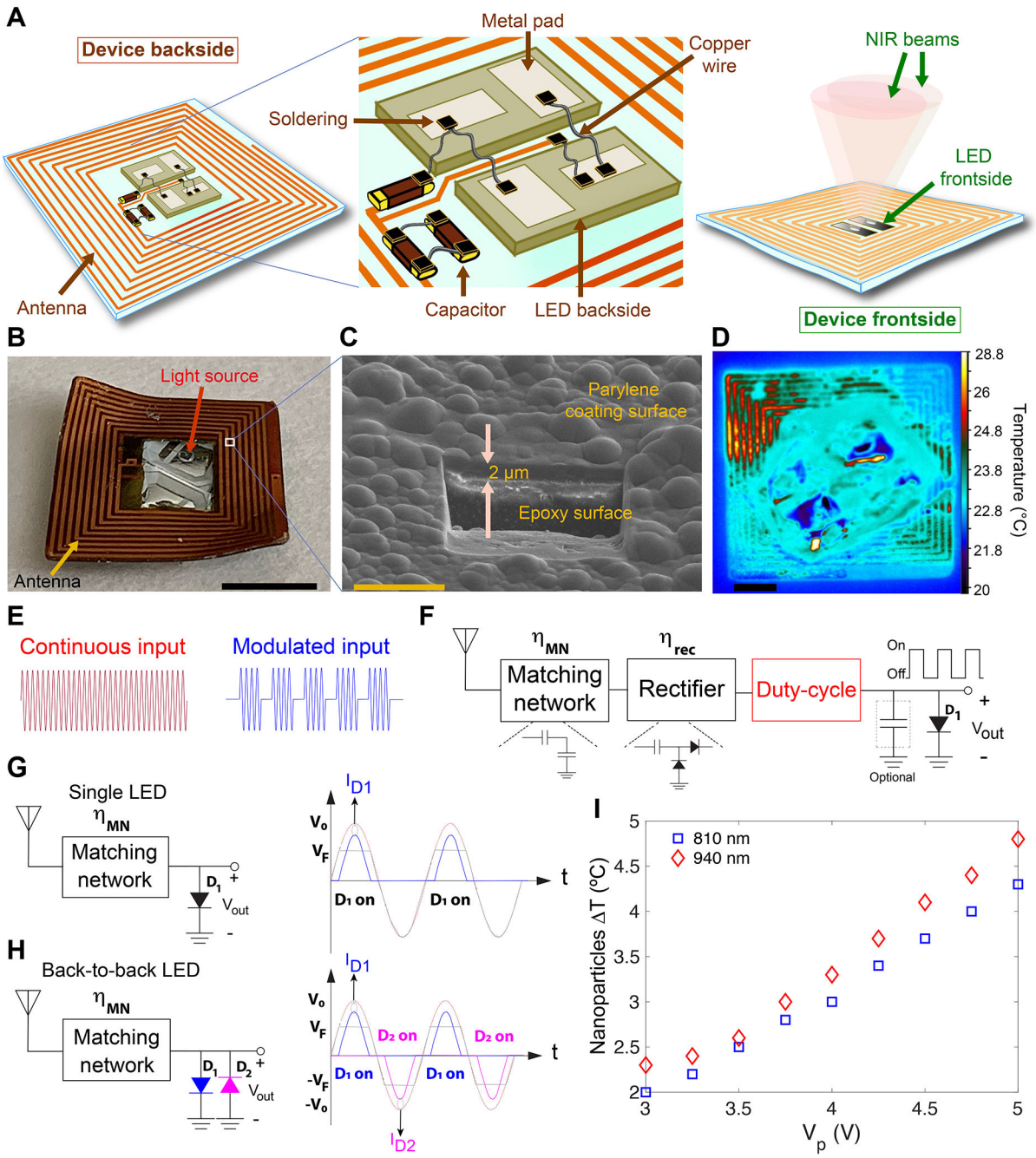

Fig. 2. Designing duty-cycled NIR-emitting devices for remotely-controlled triggering of nanoparticles photothermal effect in the brain over a long-term (15 days) treatment cycle.

(**A**) Schematics showing the backside and frontside views of the device, and circuit design and components used for their fabrication. Flexibility of the device enables its curvilinear fitting on the mouse skull. (**B** and **C**) Representative photograph of a device (scale bar: 3 mm) and scanning electron microscopy at a selected point on the surface of the device showing a 2-μm thick parylene polymer coating (scale bar: 10 μm; also see Supplementary Fig. 15). (**D**) Thermal image of a device with received power of 19 dBm at the RX coil (λ = 810 nm emission, resulting in ~3 °C temperature difference in a droplet of

nanoparticles) (scale bar: 1 mm). (**E** and **F**) Conventional approach for wireless powering of the LEDs integrating a matching network, a rectifier, and an optional energy storage capacitor along with a circuit which programs the duty-cycle of the LED. The duty-cycle can be adjusted by employing a switch which allows for a programmable duty-cycle generation (red box) using a continuous input or by modulating the incoming RF signal (red and blue waveforms in (E)). The definition and values of the device power efficiencies are provided in Supplementary Text. (**G**) Single and (**H**) back-to-back LED circuit designs used for wireless activation of nanoparticles' photothermal effect. In single LED design, the LED was only ON for half the cycle, achieving a maximum duty cycle of 31.8%. However, in the back-to-back LED topology, each LED was turned on for half the cycle, and therefore at least one LED was ON during each half-cycle. This effectively doubles the duty-cycle. (**I**) Evaluation of nanoparticles' heating effect during irradiations with 810-nm and 940-nm devices. Graph shows variations of nanoparticles' ΔT with voltage amplitude (peak voltage, V_p) with a sinusoidal input. A peak voltage of around 4 V (~ 80 mW input power) resulted in ~3 °C temperature difference in a droplet of nanoparticles deposited on top of a coverslip, due to their photothermal response. TEM analysis of the nanostars (Supplementary Fig. 8) shows their morphological stability after 15 min photothermal activation for 15 consecutive days, verifying that duty-cycled irradiation of the nanoparticles with our back-to-back LED design helped to maintain the morphology of the nanoparticles and is suitable for long-term and consistent photothermal heating in the brain.

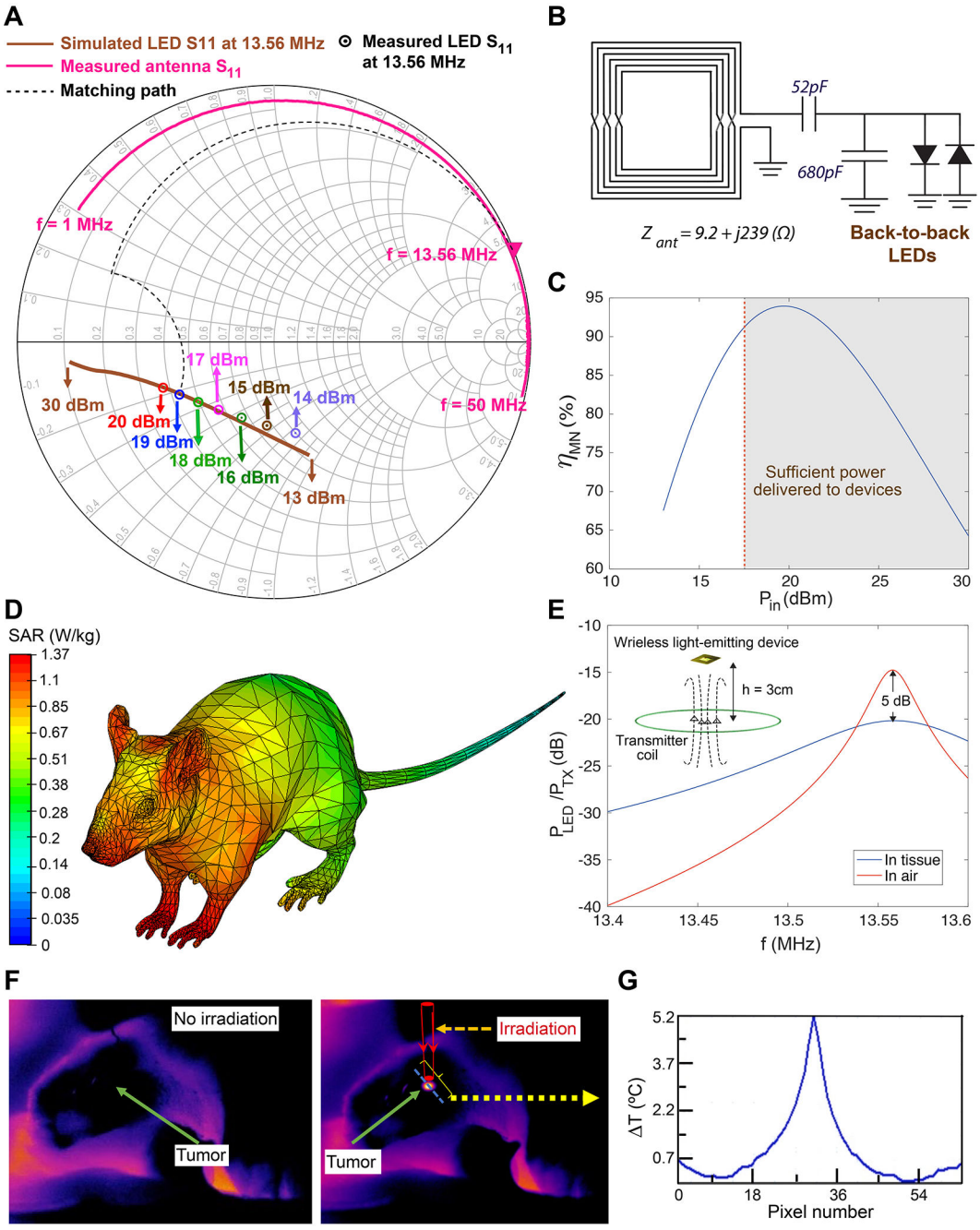

Fig. 3. Tuning wireless power transfer efficiency and evaluating safety for photothermal therapy in freely-behaving mice.

(**A**) Smith chart showing simulated and measured S_{11} for back-to-back devices with LEDs emitting 810 nm wavelength light. The measured S_{11} of the antenna is also shown along with the ideal matching path (dashed line). (**B**) L-match structure and matching components for the back-to-back devices. The 52 pF capacitance was constructed by placing two 22 pF and 30 pF capacitors in parallel. (**C**) Variation of the matching network efficiency, η_{MN}, with input power (P_{in}), assuming capacitor quality factor of Q_c=100 for the matching components. (**D**) Quantitative evaluation of mouse body interactions with 13.56 MHz RF

waves to evaluate safety of the wireless power transfer in our approach during wireless therapy cycles (compare with SAR values calculated for conventional 915 MHz RF waves in Supplementary Fig. 20). The scale bar is logarithmic. (**E**) Effect of the tissue on the wireless link efficiency (ratio of the power received at the input of the devices to the transmitted power) after implantation on the mouse skull, suggesting ~ 5 dB degradation in the power delivered to the RX antenna, due to the tissue interaction. (**F**) *In vivo* open-skull thermal images of the brain tumor, 24 h after intratumoral injection of nanoparticles. NIR emitting device was fixed above the brain (also see Supplementary Figs. 22-23). (**G**) Temperature variation along the blue dotted line on the brain shown in (F), verifying that only the tumor area which contained the nanoparticles was heated during the NIR irradiation (~30 mW), due to the nanoparticles photothermal response. We did not observe any elevated temperature in surrounding normal brain tissues.

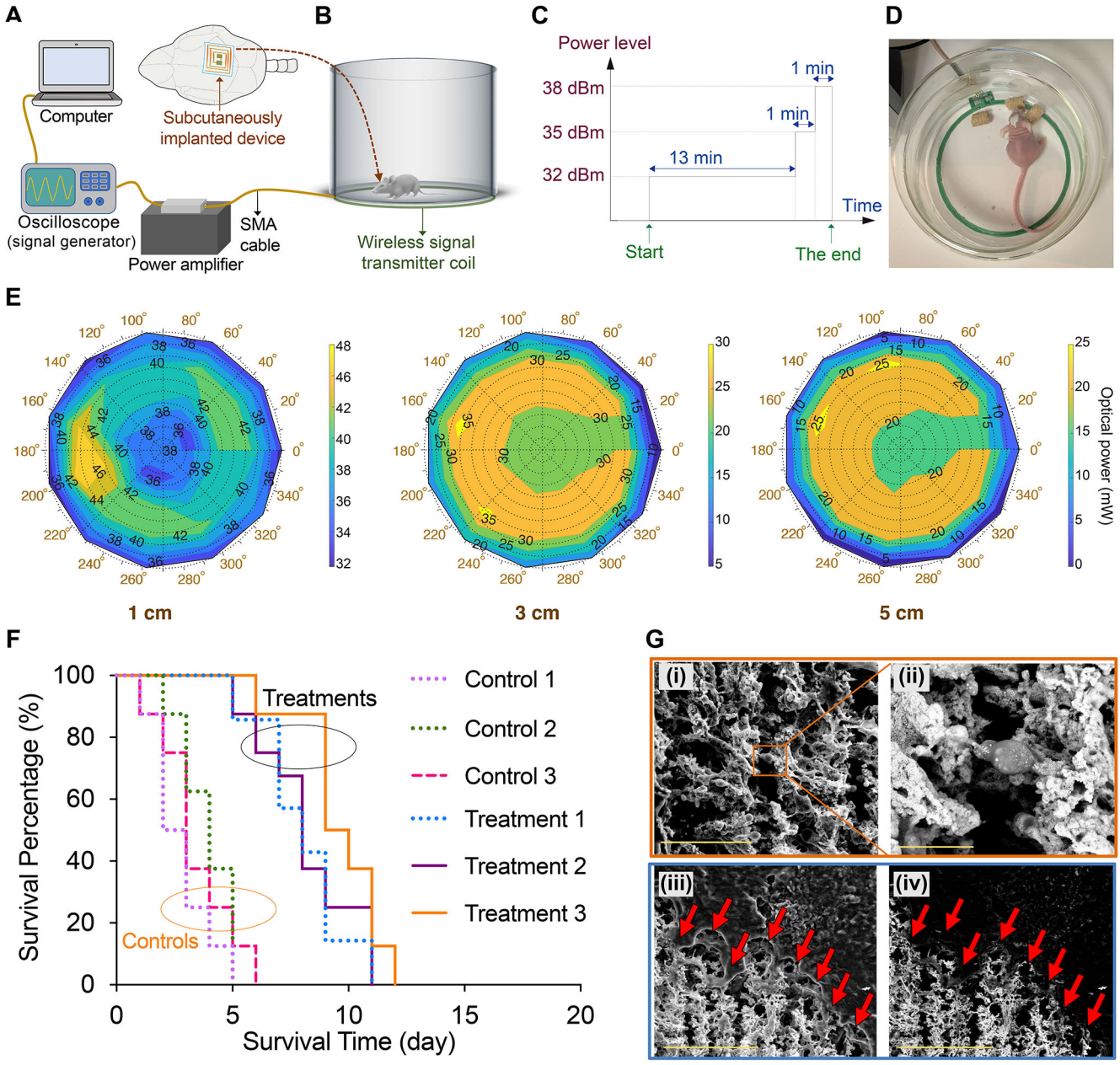

Fig. 4. Wireless photothermal therapy of brain tumors in freely-behaving mice.

(**A** and **B**) Schematic showing the computer-controlled wireless power delivery setup used for photothermal therapy of brain tumors. (**C**) Multi-level powering scheme used for continuous therapy on a daily basis for 940-nm devices (see Supplementary Figs. 24 and 30 for details). (**D**) Photograph showing a mouse eating during the wireless tumor therapy session, indicating that our approach did not disturb animal's normal behavior (also see Supplementary Fig. 25 and Supplementary Video 1). (**E**) Plots showing optical power *versus* the polar position of the NIR-emitting devices (940 nm, pre-implantation) from the center of the wireless transmitter (TX) coil to evaluate variations of the optical power with height changes to account for movement of the mice. Also, see Supplementary

Figs. 26-28 for measurement setup and other related plots for both 810- and 940-nm devices. (**F**) Survival profiles of the mice with human U87-eGFP-fLuc glioblastoma tumors treated with wireless photothermal approach (Treatment groups 1, 2, and 3) compared with control mice (n=10/group, total=60). NPs (1 μL, 0.5 nM) were injected intratumorally, and photothermal therapy was started after 24 h (15 min per day for 15 days). [Control 1: NPs (−), Implantation (−); Control 2: NPs (+), Microfiber (+), Irradiation (−); Control 3: NPs (+), Device (+), Irradiation (−); Treatment 1: NPs (+), Microfiber (+), Irradiation [810 nm] (+); Treatment 2: NPs (+), 810 nm Device (+), Irradiation (+); Treatment 3: NPs (+), 940 nm Device (+), Irradiation (+)]. Significant differences were observed when comparing each treatment group with control profiles ($p<0.05$, using the log-rank test). Also see survival results for mice with GL26 and GBM39 tumors, as well as combination therapy results in Supplementary Figs. 41-43. (**G**) Secondary electron (*i* and *iii*) and backscattered (*ii* and *iv*) SEM images of a brain section, showing photothermal effect of the nanoparticles (porous areas shown with arrows) in tumor tissue. All bright contrast spots in backscattered images (*ii* and *iv*) represent gold nanoparticles due to their enhanced electron backscattering (see Supplementary Figs. 44-48 for more detailed histological analysis of the tumors at the end of therapies). Scale bars in (*i*), (*ii*), and (*iii*-*iv*) represent 50, 10, and 100 μm, respectively.